PNAS RESEARCH ARTICLE | BIOPHYSICS AND COMPUTATIONAL BIOLOGY

Feedback linking cell envelope stiffness, curvature, and synthesis enables robust rod-shaped bacterial growth

Salem al-Mosleh[a], Ajay Gopinathan[b,c], Christian D. Santangelo[d], Kerwyn Casey Huang[e,f,g,1], and Enrique R. Rojas[h,1]

Edited by Herbert Levine, Northeastern University, Boston, MA; received March 30, 2022; accepted August 9, 2022

Bacterial growth is remarkably robust to environmental fluctuations, yet the mechanisms of growth-rate homeostasis are poorly understood. Here, we combine theory and experiment to infer mechanisms by which *Escherichia coli* adapts its growth rate in response to changes in osmolarity, a fundamental physicochemical property of the environment. The central tenet of our theoretical model is that cell-envelope expansion is only sensitive to local information, such as enzyme concentrations, cell-envelope curvature, and mechanical strain in the envelope. We constrained this model with quantitative measurements of the dynamics of *E. coli* elongation rate and cell width after hyperosmotic shock. Our analysis demonstrated that adaptive cell-envelope softening is a key process underlying growth-rate homeostasis. Furthermore, our model correctly predicted that softening does not occur above a critical hyperosmotic shock magnitude and precisely recapitulated the elongation-rate dynamics in response to shocks with magnitude larger than this threshold. Finally, we found that, to coordinately achieve growth-rate and cell-width homeostasis, cells employ direct feedback between cell-envelope curvature and envelope expansion. In sum, our analysis points to cellular mechanisms of bacterial growth-rate homeostasis and provides a practical theoretical framework for understanding this process.

cell mechanics | hyperosmotic shock | cell envelope | stored growth | envelope softening

Significance

The bacterial cell envelope is the critical structure that defines cell size and shape, and its expansion therefore defines cell growth. Although size, shape, and growth rate are important cellular variables that are robust to environmental fluctuations, the feedback mechanisms by which these variables influence cell-envelope expansion are unknown. Here, we explore how *Escherichia coli* cells achieve growth-rate and cell-width homeostasis during fluctuations in osmolarity, a key environmental property. A biophysical model in which the cell envelope softens after an osmotic shock and envelope expansion depends directly on local curvature quantitatively recapitulated all experimental observations. Our study elucidates new mechanisms of bacterial cell morphogenesis and highlights the intimate interplay between global cellular variables and the mechanisms of cell-envelope expansion.

For bacterial cells, cell growth and cellular morphogenesis are intimately related. For example, to achieve its characteristic rod shape, *Escherichia coli* must maintain its cell width (Fig. 1) while growing in cell length. Despite its complexity, this process is remarkably robust: bacterial cells maintain cell shape and cell growth with precision across environmental conditions and during dramatic environmental perturbations (1–5). Although much is known about the molecular pathways that are required for increased cell volume and surface area (6, 7), little is known about the homeostatic mechanisms that couple these processes to guarantee stable cell growth and morphogenesis. In particular, it is unknown which global (cell-scale) morphogenetic variables—such as cell width, cell length, or cell growth rate—feed back directly onto the mechanisms that orchestrate cell growth.

The genome encodes the morphogenetic machinery that synthesizes the cell envelope, which is the key structure that defines bacterial cell size and shape (8). Thus, the expansion of this surface defines cell growth and morphogenesis. The cell envelope is complex and diverse. In Gram-negative bacteria such as *E. coli*, the envelope is a multilayered structure that includes the peptidoglycan cell wall and the outer membrane (Fig. 1). Both of these layers contribute to envelope mechanical integrity, while the cell wall is the key structural determinant of cell shape (8).

Synthesis of the cell wall and the outer membrane is carried out by sophisticated molecular machineries. Assembly of the cell wall is executed by protein machineries called "Rod complexes" (9) that are distributed throughout the cylindrical (i.e., nonpolar) regions of the plasma membrane (Fig. 1) (10). Rod complexes synthesize nascent glycan polymers processively from one end and crosslink them into the existing cell wall via their free peptide stems. Integration of nascent peptidoglycan into the cell wall also requires the activity of hydrolases that cleave the existing material (11). Processive peptidoglycan synthesis is oriented approximately parallel to the circumference of the cell such that glycans are preferentially oriented circumferentially and peptides are oriented parallel to the cell axis (Fig. 1), resulting in structural anisotropy of the cell wall at the molecular scale. This structural anisotropy is thought to be critical for rod-shape maintenance by stiffening the cell envelope in the circumferential direction (12).

A few paradigmatic cases demonstrate how global morphogenetic variables can regulate molecular-scale cell envelope homeostasis. First, positioning of the cell-division septum in *E. coli* is in part governed by the spatiotemporal dynamics of the Min proteins, which depend directly on global cell-envelope geometry (13–17). Second, when *E. coli*

Author contributions: S.a.-M., A.G., C.D.S., K.C.H., and E.R.R. designed research; S.a.-M., C.D.S., K.C.H., and E.R.R. performed research; S.a.-M., A.G., C.D.S., K.C.H., and E.R.R. contributed new reagents/analytic tools; S.a.-M., A.G., C.D.S., K.C.H., and E.R.R. analyzed data; and S.a.-M., A.G., C.D.S., K.C.H., and E.R.R. wrote the paper.

The authors declare no competing interest.

This article is a PNAS Direct Submission.

[1]To whom correspondence may be addressed. Email: kchuang@stanford.edu or rojas@nyu.edu.

This article contains supporting information online at http://www.pnas.org/lookup/suppl/doi:10.1073/pnas.2200728119/-/DCSupplemental.

Published October 3, 2022.

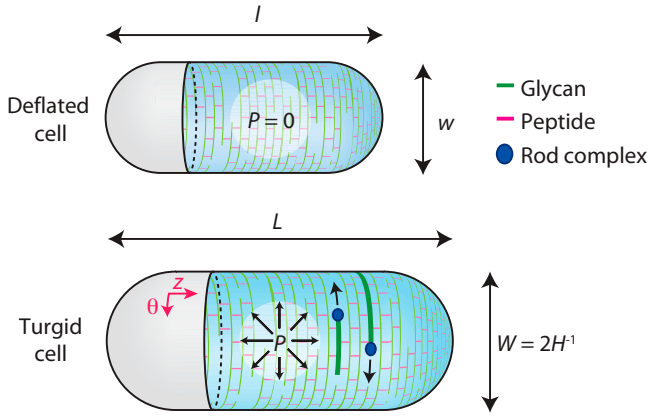

Fig. 1. Gram-negative bacterial cell geometry and mechanics. Schematic of a Gram-negative bacterial cell, illustrating its rest length l and rest width w in the absence of any applied forces such as turgor pressure. During steady-state growth with rate λ_0, turgor pressure $P(t) = P_0$ stretches the cell to length $L(t) = L(0)\exp(\lambda_0 t)$ and width $W(t) = 2H^{-1} = W_0$, where H is the curvature. Synthesis of the peptidoglycan cell wall takes place through the action of rod complexes (blue circles); glycan strands (green) are inserted in an approximately circumferential direction and crosslinked to old material through short peptides (red).

cells are temporarily constrained to adopt a bent shape within a curved channel and then released, new envelope synthesis by Rod complexes preferentially localizes to the inner curvature, which promotes cell straightening (18, 19). It is likely that this localization preference represents feedback from global cell shape via the local geometry of the cell envelope. Similarly, circumferential glycan synthesis is thought to rely on the ability of some components of the Rod complexes to sense membrane curvature (10, 20–23). According to one model, short (~100s of nm) polymers of the actin homolog MreB, which scaffold other components of the Rod complexes, align circumferentially along the direction of maximal membrane curvature and act as molecular rudders that steer glycan synthesis in this direction (24, 25). These mechanisms likely represent the tip of the iceberg with respect to how global variables feed back onto the molecular-scale machinery of cellular morphogenesis.

Ultimately, cellular morphogenesis requires physical cell inflation, yet the ways in which mechanical forces interact with the molecular mechanisms of morphogenesis are not understood. A key question is the role of turgor pressure, another global variable, in promoting cell-envelope expansion during cell growth (Fig. 1) (26). Turgor pressure, which results from the osmotic pressure differential across the plasma membrane, pushes the membrane against the cell wall (27). In principle, turgor pressure could feed back onto cell-envelope expansion in two ways: (i) by activating the enzymes that carry out synthesis and/or hydrolysis of the cell envelope or (ii) by direct plastic deformation of the envelope. Importantly, turgor pressure could influence cell-wall expansion indirectly through the degree to which the envelope is stretched (the mechanical strain) or envelope curvature; both of these local variables are dependent on the degree to which the cell is inflated by turgor pressure.

To address the role of turgor pressure in cell-envelope expansion, in a previous study, we measured the growth-rate dynamics of *E. coli* in response to osmotic shocks (acute changes in extracellular osmolarity that alter turgor pressure) (3). The responses were complex: while modest hyperosmotic shocks (<300 mM in magnitude) clearly reduced single-cell growth rate, when turgor pressure was re-established by reversing the shock, cells rapidly elongated to the size that they would have had in the absence of the shock (3). That is, the cells appeared to "store growth" during the period of reduced growth rate. Although similar phenomena have been observed in the alga *Chara corallina* (28), the mechanisms that enable stored growth and the conditions under which it can be achieved are not well understood.

To understand stored growth and the interplay of cell morphology, cell envelope synthesis, and turgor pressure more broadly, we developed a generic theory for the expansion of a thin pressurized shell (29) that unifies these processes. We validated this model using an extensive dataset concerning cellular elongation rate and cell-width dynamics after osmotic shocks. The central underlying tenet of our model is "locality": that the rate of cell-envelope expansion depends only on local information, including the rate of cell-envelope synthesis, cell-envelope curvature, and mechanical strain in the envelope. We found that the model can only explain stored growth if it includes adaptive cell-envelope softening, which also accelerates recovery of cell width. Moreover, the model successfully predicts a threshold shock magnitude above which stored growth cannot occur due to an instability generated by envelope softening. Beyond this shock magnitude, the model quantitatively predicts the slope of the experimentally observed linear decrease in elongation rate as a function of shock magnitude. Finally, we found that direct feedback between envelope curvature and envelope expansion is required to explain the transient dynamics of cell length and width after hyperosmotic shock. These results highlight the sophisticated nature of the feedback system that governs cellular morphogenesis, which coordinately controls cell-elongation rate and cell width by coupling them to envelope stiffness and synthesis; the specific organization of this feedback system promotes robust and rapid homeostasis of each of these variables.

Results

A Physical Model of Surface Expansion Based on the Principle of Locality Can Be Adapted to Bacterial Growth. Our strategy for interrogating bacterial morphogenesis was to derive a mathematical model that is generic enough to capture the rich phenomenology of cell-growth dynamics upon perturbation, constrain this model with a broad set of experimental data, and infer principles of morphogenesis from these constraints. Motivated by a large body of experimental support, we chose to derive a coarse-grained model of cell-envelope expansion based on the principle of locality. Here, locality implies that envelope expansion at a given point is only dependent on information within its immediate microscopic vicinity. Such information could be chemical (e.g., local enzyme concentration), mechanical (e.g., mechanical strain in the cell envelope), or geometrical (e.g., curvature of the cell envelope). Within this framework, global (cell-scale) information can only be sensed insofar as it is coupled to local information. For example, the width of a rod-shaped cell could only be sensed indirectly through local curvature since these two variables are inversely related (Fig. 1). Similarly, turgor pressure could be sensed indirectly through local mechanical strain.

Based on this principle, we adapted a differential geometry-based theory for the expansion of thin elastic surfaces to rod-shaped (cylindrical) cell-envelope expansion (30) (*Methods and Materials* and *SI Appendix*). The dynamics of cell growth are described by those of the rest-metric tensor, $g_{ij}(t)$; along with the rest-curvature tensor, $b_{ij}(t)$, the rest-metric tensor specifies the geometry of the cell envelope when there are no external forces applied to it (*SI Appendix*, Fig. S1). In the presence of turgor pressure, the envelope stretches (Fig. 1) and its geometry is described by the metric tensor $G_{ij}(t)$ and curvature tensor

$B_{ij}(t)$. Generically, the dynamics of the rest-metric tensor may depend on envelope curvature and mechanical strain in the envelope (*SI Appendix*, Fig. S1). We performed a Taylor expansion of metric-tensor dynamics to leading orders of curvature and strain, motivated by the fact that the curvature of the cell envelope (inverse radius of curvature) is small compared with the inverse of the size of molecular components, such as MreB. We identified four key terms that could affect cell morphology dynamics after hyperosmotic shock (*SI Appendix*):

$$\underbrace{\frac{1}{\lambda_0}\frac{\partial g_{ij}}{\partial t}}_{\text{Expansion rate}} = \underbrace{A_{ij}}_{\text{1. Envelope synthesis}} + \underbrace{\frac{\alpha_1}{2{H_0}^2}(H-H_0)B_{ij}}_{\text{2. Cell-width homeostasis}} - \underbrace{\frac{\alpha_2}{2H_0}(H-H_0)G_{ij}}_{\text{3. Width-elongation coupling}} + \underbrace{\beta S_{ij}}_{\text{4. Mechanical expansion}}. \quad [1]$$

The left-hand side of Eq. **1** is the time derivative of the rest-metric tensor, which defines the expansion rates of the cell envelope in both principal directions (longitudinal and circumferential, denoted z and θ, respectively, in Fig. 1); λ_0 defines the steady-state rate of exponential elongation (31–34).

Term 1 on the right-hand side of Eq. **1** represents steady-state anisotropic expansion of the cell surface along the principal curvature directions (*SI Appendix*). Biologically, this term corresponds to the expansion of the cell surface that results from curvature-dependent anisotropic synthesis of envelope material.

Terms 2 and 3 encompass direct feedback between cell-envelope curvature, H, and cell-surface expansion. H is positive by convention. $H_0 = 2/W_0$ is the steady-state envelope curvature where W_0 is the steady-state cell width. α_1 and α_2 are proportionality constants. For a cylindrical cell, only the circumferential component of the curvature tensor $B_{ij}(t)$ is nonzero. Term 2 by itself ensures cell-width homeostasis by providing negative feedback between circumferential curvature and circumferential expansion. Term 3 modulates isotropic surface expansion in an envelope curvature-dependent manner. Biologically, these two terms could rely on a single process, for example, curvature-dependent localization of Rod complexes (10).

Term 4 corresponds to irreversible cell-surface expansion driven directly by mechanical strain in the cell envelope, which results from turgor pressure. This term yields anisotropic expansion that is directly proportional to the anisotropy in the strain tensor, $S_{ij}(t) = (G_{ij}(t) - g_{ij}(t))/2$, where β is a proportionality constant. Notably, this term is not the only mechanism by which envelope expansion could depend on strain: since terms 1–3 prescribe changes in the rest-metric tensor that explicitly depend on envelope shape, and since shape changes in response to mechanical forces, the elongation rate implicitly depends on strain, even when $\beta = 0$.

A minimal version of the model with terms 1 and 2 alone can achieve stable rod-shaped elongation: a cylinder with constant width equal to $2/H_0$ and exponentially increasing length $L(t) = L(0)\exp(\lambda_0 t)$ is a steady-state solution of Eq. **1** (*SI Appendix*). To determine whether contributions from terms 3 and 4 are required to explain the dynamics of cell morphogenesis in general, we sought to perturb cell growth from its steady-state behavior. We did so by subjecting cells to hyperosmotic shock, which rapidly changes the curvature and mechanical strain in the cell envelope. This strategy allowed us to directly test whether cell elongation and cell width are coupled due to curvature-dependent cell-envelope expansion and whether mechanical strain directly drives cell-envelope expansion.

Stored Growth Implicates Dynamic Adaptation of Cell-Envelope Stiffness. When *E. coli* cells are perfused constantly with rich medium, they elongate at a steady-state rate of $\lambda_0 = d(\ln L)/dt \sim 0.03\ \text{min}^{-1}$. Stored growth occurs when cells are subjected to modest (≤300 mM), transient hyperosmotic shocks (5). During hyperosmotic shock, turgor pressure decreases and the cell envelope contracts (Fig. 2 *A* and *B*), with envelope length governed by linear elasticity:

$$L(t) = \left(1 + \varepsilon_0 \frac{p}{\gamma(t)}\right) l(t), \quad [2]$$

where $l(t)$ is the rest length of the cell, $p = P/P_0$ is the turgor pressure normalized by its steady-state value, $\gamma(t) = Y(t)/Y_0$ is Young's modulus of the cell envelope normalized by its steady-state value, and ε_0 is the mechanical strain in the cell envelope prior to the decrease in turgor pressure. In previous work, we measured $\varepsilon_0 = 0.1 \pm 0.03$ (SD) (35). Immediately after a hyperosmotic shock, cells elongate slower than before. However, the cells store growth: when the shock is reversed, cells rapidly expand elastically to the size that they would have attained during this period had they never been subjected to the shock (Fig. 2*B*) (3).

To achieve stored growth, the elastic expansion when the shock is reversed (i.e., during the "downshock", Fig. 2 *A* and *B*) must necessarily be larger than the elastic contraction when the shock is applied ("upshock", Fig. 2 *A* and *B*) to make up for the slower elongation during the period of reduced turgor pressure (Fig. 2 *B*–*D*). This difference means that the cell envelope is less stiff at the end of the period of low turgor than directly after the hyperosmotic shock. The condition for stored growth—that the reversal of the shock fully compensates for the length lost during low turgor—leads to an expression for the dynamics of the longitudinal Young's modulus after hyperosmotic shock, $\gamma(t)$,

$$\gamma(t) \approx \frac{(1-p)\varepsilon_0}{\delta L(t)}, \quad [3]$$

where $\delta L(t) \equiv \frac{L(t)-L_0(t)}{L_0(t)}$ is the relative difference between the cell length, $L(t)$, and the length that the cell envelope would have had in the absence of perturbation, $L_0(t)$. As this difference increases, the longitudinal Young's modulus decreases. There are no fitting parameters in Eq. **3**; hence, $\gamma(t)$ is a direct consequence of the dynamics of $L(t)$.

We estimated the theoretical rate and extent of softening upon hyperosmotic shock by solving Eqs. **1–3**. By substituting the predicted length dynamics into Eq. **3**, we predicted the time evolution of longitudinal Young's modulus after the hyperosmotic shock (Fig. 2*E*). By comparing the mechanical strains induced by hyperosmotic shock and reversal of the shock (Fig. 2 *A*–*D* and *SI Appendix*, Fig. S2), we found that during the 60 s after a 100-mM hyperosmotic shock the elastic modulus decreased by 19 ± 6%, in reasonable agreement with the prediction of 10% after a normalized time $\lambda_0 t = 0.033$ from our model (Fig. 2*E*). Remarkably, our model predicted that longitudinal Young's modulus would decrease by >25% during one cell cycle in the absence of osmoregulation (Fig. 2*E*).

Envelope softening can be viewed as a mechanical mechanism of sensing global cellular dimensions. Specifically, envelope softening intrinsically records the deviation between global cell length and the length determined by cell-envelope synthesis (i.e., δL).

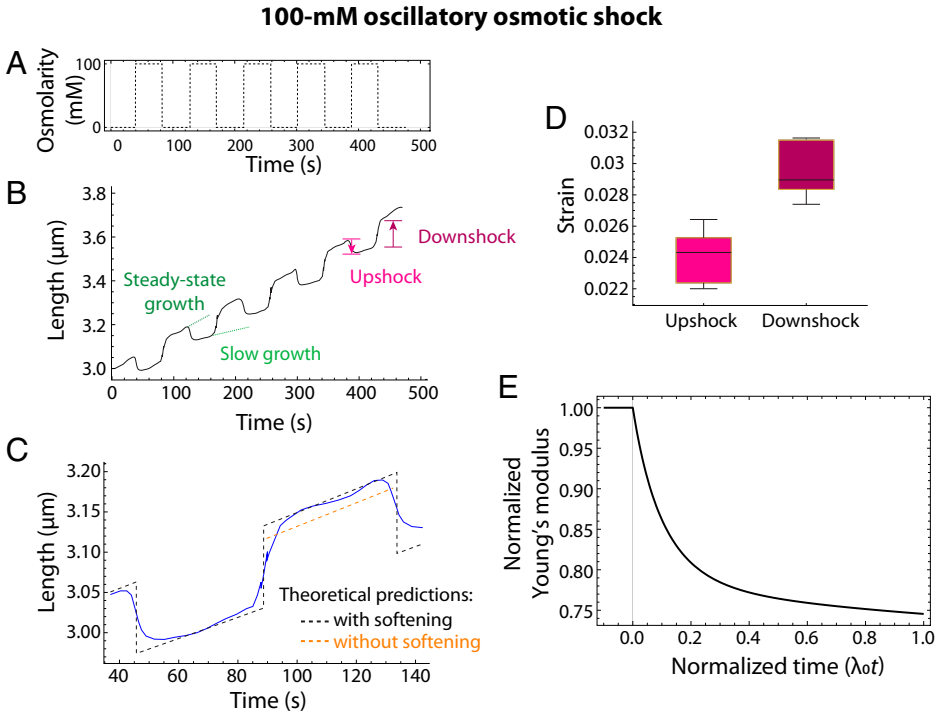

Fig. 2. Stored growth during cycles of hyper- and hypo-osmotic shocks can be explained by cell envelope softening. (*A*) Osmolarity as a function of time. (*B*) Experimentally measured cell-length dynamics (black) in response to cycles of 100-mM hyper- and hypoosmotic shocks demonstrate stored growth: immediately after the hyperosmotic shocks, growth rate decreases, yet after the hypoosmotic shocks, cell length ends up matching the predicted elongation in unperturbed conditions extrapolated from the initial cell length and growth rate. (*C*) A closer look at a portion from panel *B*. Orange dashed curve shows the predicted dynamics after the hypoosmotic shock in the absence of envelope softening. (*D*) The mechanical strain induced by the hyperosmotic shocks in *B* is smaller than the strain induced by the hypoosmotic shocks, implying softening of the cell envelope. (*E*) Model prediction of the envelope softening necessary for stored growth after a 100-mM hyperosmotic shock is in reasonable agreement with the softening inferred from the mechanical strain data as discussed in the text.

Furthermore, softening intrinsically provides a mechanical mechanism to reduce this deviation.

Cell-Envelope Softening and Curvature Feedback Enable Simultaneous Homeostasis of Cellular Elongation Rate and Cell Width. We next hypothesized that cell-envelope softening would affect elongation-rate dynamics on longer time scales after single hyperosmotic shocks (without reversing the shock). To test this hypothesis, we used microfluidics to subject *E. coli* cells growing at steady state to hyperosmotic shocks across a wide range of magnitudes and measured the dynamic responses of cell length over time. We then systematically tested these data against our model (Eq. **1**), with and without envelope softening (Eq. **3**). Throughout our entire analysis, we used a single set of model parameters to explain experimental data (*Methods and Materials*).

By quantifying the relative length difference, $\delta L(t)$, and the relative difference between the observed elongation rate and the elongation rate before the shock, $\delta\lambda(t) = (\lambda(t) - \lambda_0)/\lambda_0$, we found that the shock caused a short, transient period of reduced elongation rate (Fig. 3 *A*–*C*), followed by rapid re-establishment of the preshock elongation rate (Fig. 3*C*). In the absence of envelope softening, both the minimal version of our model (the "minimal model"; Eq. **1**, terms 1 and 2) and the version that includes feedback from envelope curvature (the "curvature-feedback model"; Eq. **1**, terms 1–3) poorly predicted the experimental cell-length dynamics after hyperosmotic shock (Fig. 3 *A* and *B*). Each model generically predicted that the relative length change, $\delta L(t)$, does not approach a constant value (Fig. 3*B*) and equivalently that the relative elongation rate change, $\delta\lambda(t)$, does not approach zero (Fig. 3*C*), in contrast to our experimental observations (Fig. 3 *B* and *C*). When combined with softening (Eq. **3**), however, the curvature feedback model accurately captured the length dynamics after both a 400-mM (Fig. 3 *A*–*C*) and a 200-mM shock (*SI Appendix*, Fig. S3), while the minimal model did not (Fig. 3 *A*–*C* and *SI Appendix*, Fig. S3). The minimal model predicted a smaller initial decrease in elongation rate than in experiments, and the relative rate change was approximately constant over the interval during which the curvature model exhibited adaptation (Fig. 3*C*). In sum, these findings implicate direct dependence of cell elongation on envelope curvature and point to the critical role of envelope softening during adaptation to changes in turgor pressure.

The role of softening in elongation-rate homeostasis is straightforward to understand mechanistically. First, the reduction in turgor pressure caused by the hyperosmotic shock causes the cell to contract. In our curvature-feedback model, this decrease in pressure leads to a reduced elongation rate (directly after the shock) due to contributions from term 1 (Eq. **1**), as the contraction reduces the available amount of surface area into which new material is being inserted for a given rest state, and term 3, as elongation rate responds to the turgor-induced decrease in width. As elongation rate decreases, however, and the relative length change increases in magnitude, softening of the envelope allows the reduced turgor pressure to adaptively stretch the envelope to the extent that it was stretched before the shock, thereby re-establishing the steady-state elongation rate. In the minimal model, softening also leads to growth-rate adaptation, but on a much longer time scale (Fig. 3*C*).

We identified further evidence for our curvature-feedback model by comparing its predictions with experimental cell-width dynamics. Hyperosmotic shock caused a rapid reduction in width (Fig. 3*D*), followed by a rapid recovery (Fig. 3*D*) on the same time scale as elongation-rate recovery (Fig. 3*C*). Using the same set of model parameters as was used to fit elongation

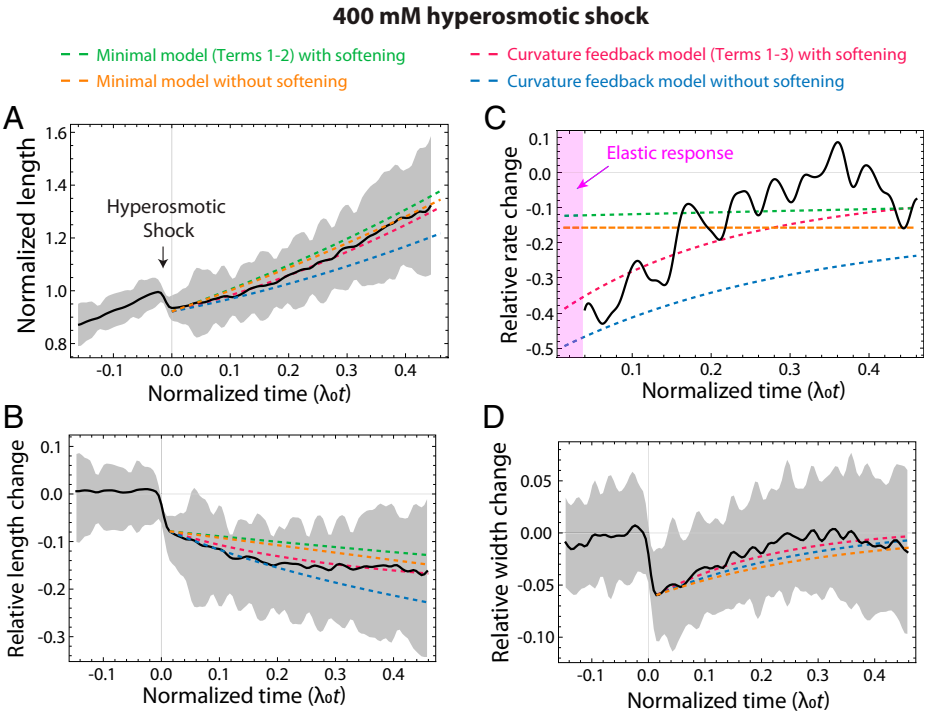

Fig. 3. Model with envelope softening predicts homeostasis of growth rate and cell width in response to hyperosmotic shock. (*A*) The response dynamics of cell length to a 400-mM hyperosmotic shock predicted by our model with envelope softening and curvature feedback (red) were in close agreement with experimental measurements (black). Shaded region represents 1 SD. Parameter estimates were obtained as described in the *Methods and Materials*. The predictions from the model without curvature feedback and without envelope softening are shown for comparison. (*B*) The predicted relative cell-length change dynamics for the data in *A* are in close agreement with experimental measurements. The initial decrease is $\delta L(0) = -0.08$. The predictions from the model without curvature feedback and without envelope softening are shown for comparison. (*C*) The rapid recovery of growth rate to its preshock value (black) is predicted by our curvature-feedback model with envelope softening. The initial interval just after the shock (pink) was dominated by the elastic response. (*D*) Width initially shrank elastically after the hyperosmotic shock due to the decrease in turgor pressure but then recovered back to its preshock value within approximately one cell doubling. The transient dynamics and recovery are due to the presence of curvature coupling in our model.

rate and length dynamics (Fig. 3 *B* and *C*), both our curvature-feedback model and the minimal model predicted this qualitative width recovery (with or without softening) (Fig. 3*D*). Both softening and curvature feedback were predicted to accelerate width recovery, and the combination of both led to close agreement with experimental measurements (Fig. 3*D*).

Softening-Mediated Elongation-Rate Homeostasis Is Unstable for Large Hyperosmotic Shocks. Thus far, we have focused on scenarios in which turgor pressure remains positive after the hyperosmotic shock. Within our model, if a hyperosmotic shock is large enough to cause turgor pressure to fall below zero, softening combined with the compressive forces in the cell envelope due to negative turgor pressure would lead to growth arrest rather than promoting recovery of elongation rate. In the language of our model, the dynamics of deviations of cell length and width from their steady-state values depend on turgor pressure, and these deviations grow indefinitely for negative pressures (Fig. 4*A*). This instability is also manifested by considering the relative length and width behavior at long times as pressure goes to zero, which is predicted by our curvature feedback model to be

$$\lim_{t\to\infty} \frac{W(t) - W_0}{W_0} \equiv \lim_{t\to\infty} \delta W(t) = 0, \qquad [4]$$

$$\lim_{t\to\infty} \frac{L(t) - L_0(t)}{L_0(t)} \equiv \lim_{t\to\infty} \delta L(t) = \frac{\delta L(0)}{p}. \qquad [5]$$

That is, width recovers to its preshock steady-state value, while the relative difference between cell length and the length prescribed by steady-state elongation diverges as $p \to 0$.

Based on this analysis, we hypothesized that cells do not soften after large hyperosmotic shocks, either because cells actively inhibit softening or because the cell-envelope synthesis machinery can no longer function, and thus, we explored this regime experimentally. Remarkably, the relative difference between the steady-state elongation before and after hyperosmotic shock exhibited a sharp discontinuity at a critical shock magnitude (Fig. 4*B* and *SI Appendix*, Fig. S4). For all shocks <700 mM, elongation rate recovered to its unperturbed value (consistent with envelope softening). Conversely, for larger shocks, cells continued to grow (in contradiction to model predictions with envelope softening) but eventually stabilized at an elongation rate that decreased linearly with shock magnitude (Fig. 4*B*). This behavior was in quantitative agreement with our theory. Specifically, our curvature-feedback model without softening predicts that the slope of the linear dependence between elongation rate and shock magnitude is twice the slope of envelope strain as a function of shock magnitude (*Methods and Materials*). This model prediction of $2 \times -0.14 = -0.28$ (Fig. 4 *B* and *C*) is in reasonable agreement with the experimental slope of -0.35 ± 0.07. According to our theory, this linear decrease arises because of indirect mechanical effects of turgor pressure on elongation rate via cell-envelope geometry. That is, reduction in turgor pressure causes a decrease in cell surface area, which reduces elongation rate by reducing the amount of cell-envelope synthesis via term 1 in Eq. **1**.

For shocks with magnitude above the 700-mM threshold, direct feedback between envelope curvature and envelope expansion (Eq. **1**, term 3) was critical for explaining the dynamics of cell length. The minimal model with only terms

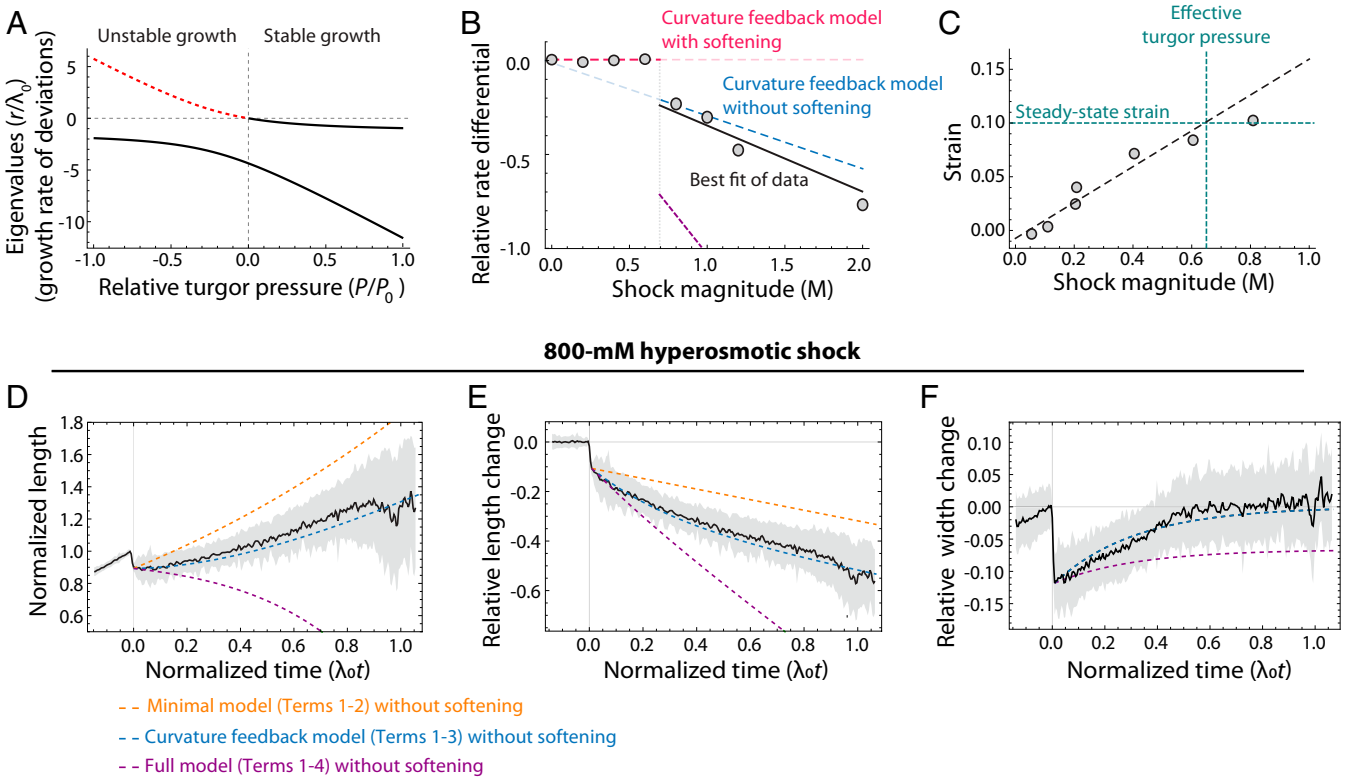

Fig. 4. Envelope softening results in an instability for large hyperosmotic shocks. (*A*) Eigenvalues that dictate the growth or decay of modes of Eqs. **10** and **11**. When $P < 0$, one eigenvalue becomes positive, indicating an unstable mode. (*B*) For hyperosmotic shocks below ~700 mM in magnitude, cells recovered to their preshock growth rate λ_0. For shocks >700 mM, cells equilibrated to a new growth rate λ_f that decreased with shock magnitude (*SI Appendix*, Fig. S4). The relative rate change is $(\lambda_f - \lambda_0)/\lambda_0$. The dashed lines show our model prediction with envelope softening (for shocks <700 mM) and without (for shocks >700 mM), which is in close agreement with the experimental data (gray circles). The purple line represents the prediction from the model in the presence of strain sensing ($g_3 = 2$). (*C*) Magnitude of the elastic length strain after hyperosmotic shocks of various magnitudes. The length strain reaches the value $\varepsilon_0 = 0.1$ (the estimated envelope strain during steady-state growth) at an estimated shock magnitude of ~700 mM. (*D*) After the 800-mM hyperosmotic shock, length increased much more slowly than the predicted rate for an unperturbed cell. Model predictions with fixed Young's modulus (blue) are in close agreement with experimental data (black). (*E*) Since growth rate decreased after the shock and remained below its unperturbed value, the relative length change $\delta L(t)$ continued to decrease from its initial value of −0.11 directly after the shock to an asymptote of −1. In the absence of curvature feedback (orange), the same final growth rate is attained as with curvature sensing, but the predicted transient behavior does not agree with experimental data (black), providing evidence that length is coupled to width through curvature feedback. (*F*) Cell width recovers to its preshock value after an 800-mM shock. The close fit of our model (blue dashed curve) to experimental data (black) provides an estimate of the model parameters $g_1 = 3.2$ and $g_3 = 0$. In the presence of strain sensing ($g_3 = 2$), our model predicts that width would not recover to its preshock value (purple).

1 and 2 failed to predict the transient length and elongation dynamics after the shock, which were precisely explained by our curvature-feedback model (Fig. 4 *D* and *E* and *SI Appendix*, Fig. S5). Together, these data suggest that envelope softening and stored growth do not occur for large-magnitude shocks and provide further support that envelope expansion is directly dependent on envelope curvature.

What is the origin of the 700-mM threshold? Within our model, this threshold is simply the steady-state turgor pressure in units of osmolarity. Interestingly, 700 mM corresponds to a large pressure of ~18 atm ($P = RT\Delta C$). By comparison, atomic force microscopy (AFM) methods measured the turgor pressure of *E. coli* to be ~1–3 atm (36), which is consistent with our previous observation that cells plasmolyze for shock magnitudes ≥100 mM (equivalent to 2.6 atm) (3). However, we identified a surprising caveat to these measurements: the cell envelope clearly continues to contract linearly for shock magnitudes up to 700 mM (Fig. 4*C*) (3). In other words, even though turgor pressure is zero after shocks >100 mM, the cytoplasm still induces tensile stress in the envelope unless the shock is >700 mM; the degree of contraction was maintained when the shock magnitude was increased from 700 mM to 3 M (35). Since this tensile stress, and not turgor pressure itself, is the key variable that is relevant to cell-envelope expansion, we define the effective turgor pressure as 700 mM, which precisely agrees with the critical shock magnitude above which we observe the discontinuity in steady-state growth rate (Fig. 4*B*) and predict that cell-envelope softening is abolished.

Envelope Expansion Is Not Explicitly Dependent on Mechanical Strain. In all the above analyses, it was unnecessary to invoke an explicit dependence of envelope expansion on envelope strain (Eq. **1**, term 4). In fact, with inclusion of this dependence, our model predictions are inconsistent with experimental measurements (Fig. 4 *B*–*F*). Under explicit strain-dependent envelope expansion, altering pressure shifts the steady-state width, which thus recovers to a different value after the shock compared with the preshock width (Fig. 4*F* and *Methods and Materials*). Furthermore, inclusion of strain-dependent expansion led to poor predictions of the elongation-rate dynamics for shock magnitudes above the critical threshold (Fig. 4*B* and *Methods and Materials*). In contrast, the successful prediction of both these behaviors by our model in the absence of term 4 in Eq. **1** provides support for the curvature-feedback model without explicit strain dependence.

Discussion

By combining theory and experiment, we identified two functional relationships between key cell-scale variables that promote

homeostasis during cell morphogenesis: (i) softening of the cell envelope due to mismatch between elongation rate and envelope-synthesis rate and (ii) the direct dependence of cell-elongation rate on envelope curvature (curvature feedback). These two relationships are both required to guarantee the experimentally observed homeostasis in cell-growth rate (Fig. 3 *A*–*C*), while only curvature feedback is required to guarantee cell-width homeostasis (Figs. 3*D* and 4*F*), although softening does accelerate width recovery after a shock (Fig. 3*D*). Our complete model (Eqs. **1**–**3**) suggests that *E. coli* morphogenesis relies on interlocking negative feedback loops linking three key cellular-scale variables: cell width, cell length, and envelope stiffness (Fig. 5*A*). Negative feedback has been demonstrated to increase stability and accelerate the response of control systems (37), underscoring the likely fitness advantages of homeostatic mechanisms during cell morphogenesis.

In our model, the interactions between cell-scale morphogenetic variables (Eq. **1** and Fig. 5*A*) must be mediated by molecular-scale properties, such as cell-envelope synthesis and envelope curvature. Our results point to potential molecular mechanisms that underlie these interactions. With respect to cell-envelope softening, we previously speculated that molecular-scale wrinkling of the cell envelope could account for stored growth (3). In this picture, which is consistent with our theory of envelope softening, hyperosmotic shock reduces elongation rate more than it reduces the rate of cell-envelope synthesis. As a result, new cell-envelope synthesis wrinkles as it is inserted into the cell wall (Fig. 5*B*). This wrinkled material results in envelope softening, since tensile forces will tend to unwrinkle it prior to stretching. Intuitively, in a toy model in which the cell envelope is represented by a chain of linear springs, if new wall material inserted during the period of hyperosmotic shock is represented by springs with lower effective spring constant and rest length, they will gradually soften the cell over time (*SI Appendix*). Furthermore, this model predicts that, when pressure is restored, the wrinkled springs revert to their unperturbed configuration with higher rest length and spring constant, leading to stored growth consistent with Eq. **3**. Alternatively, cell-envelope softening could also occur actively through tension-dependent activity of hydrolases that cleave peptide crosslinks (11), which are typically aligned longitudinally (38, 39).

One plausible mechanism for feedback between envelope curvature and envelope expansion (Eq. **1**, terms 2 and 3) would be curvature-dependent localization of the rod complexes. Rod complexes play a key role in cell elongation by coordinating peptidoglycan synthesis, and alteration of their activity in *Bacillus subtilis* changes cell width (21) via an unknown mechanism. Our model suggests that, if the binding affinity of rod complexes increases as envelope curvature decreases, wider cells would tend to simultaneously thin and elongate faster (Fig. 5*C*).

An interesting finding in our study is the disparity between the hyperosmotic shock magnitude at which cells plasmolyze (~100 mM) and that at which the cell envelope reaches its rest state (~700 mM). We speculate that this disparity is a direct result of two cellular features: the stiffness of the cytoplasm and the strong mechanical connections between the cytoplasmic (inner) membrane and the cell envelope. If the cytoplasm is both relatively stiff and connected to the cell envelope, then hyperosmotic shocks between 100 mM and 700 mM could cause compression of the cytoplasm/cell envelope complex. In this case, the inner membrane would be balancing tensile forces in the cell envelope with shear forces between the two structures. This question will be an interesting topic for future study.

It remains unclear what prevents cells from implementing envelope softening for high-magnitude shocks. For such shocks, the substantial plasmolysis (separation of the cytoplasm from the cell wall) may inhibit wall synthesis by preventing the wall synthesis and/or hydrolase enzymes from reaching from the inner membrane to the cell wall. Our model predicts that the transition away from softening occurs at a shock magnitude of ~700 mM, which may represent the point at which there is no tension in the cell envelope (but substantial compression of the outer membrane (35)). At this point, it may no longer be possible to synthesize material that can be softened, due to sensitivity of any component of the wall-synthesis machinery (synthetases or hydrolases) to wall tension. Future experiments that localize synthesis-machinery dynamics with superresolution during osmotic perturbations may resolve this question.

Homeostasis of cellular morphogenesis is a critical process in most (if not all) cells. The systems that guarantee this homeostasis must inherently incorporate molecular-scale and cell-scale information. Here, we provided a paradigm for this integration

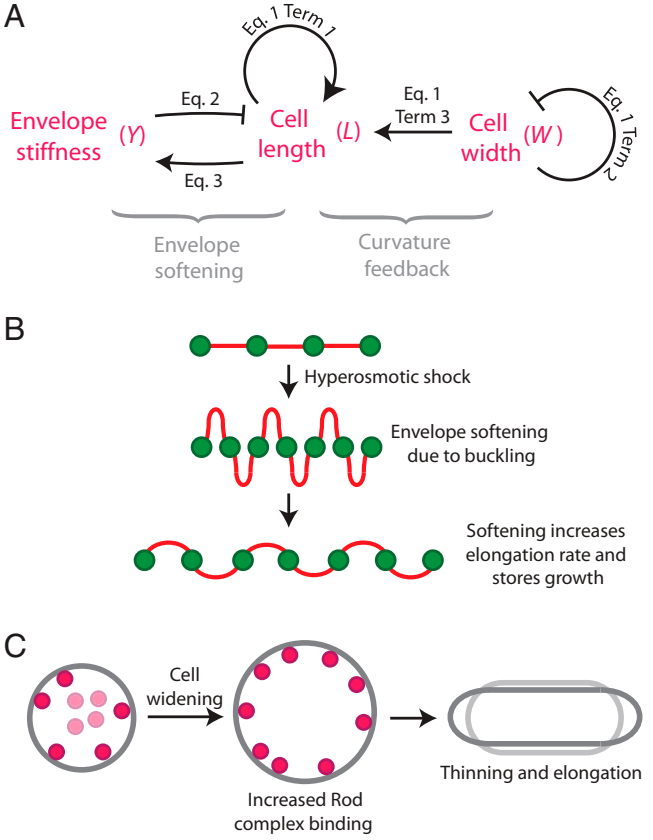

Fig. 5. Feedback linking cell length to envelope stiffness and envelope curvature leads to growth rate and width homeostasis. (*A*) Summary of model findings. During steady-state growth, cell length increases exponentially due to term 1 in Eq. **1**, and term 2 ensures width homeostasis. After a hyperosmotic shock is applied, pressure is reduced, which affects length and width through elastic stretching as well as through coupling between width and length via term 3 in Eq. **1**. Envelope stiffness inhibits elongation through Eq. **2**, and a hyperosmotic shock induces softening through Eq. **3**. The softening mechanism is assumed to only be active when the effective turgor pressure is positive to avoid the predicted instability (Fig. 4*A*). Softening compensates for the decrease in width and growth rate after the shock and leads to growth-rate homeostasis. (*B*) Toy model of softening mechanism. After a hyperosmotic shock, newly inserted cell-wall material could be wrinkled and hence would be softer than fully stretched material and thereby reduce the cell-envelope Young's modulus. (*C*) Toy model illustrating curvature feedback. Enzymes responsible for envelope synthesis may prefer binding to certain local curvatures, such that cell widening promotes increased activity that leads to simultaneous thinning and elongation.

for one of the best-studied model organisms. One high-level takeaway from our analysis is that this homeostatic system is complex: maintenance of cell width and elongation rate cannot be decomposed into component systems but are intimately coupled (Fig. 5*A*). Our model can be used to determine whether *E. coli* cells utilize the same homeostatic mechanisms under other growth conditions, and it will be interesting to compare parallel systems in other organisms with other cellular morphologies to test the generality of this architecture.

Methods and Materials

Growth Media. Concentrated growth medium was made by adding sorbitol (Sigma-Aldrich) to lysogeny broth (LB) (10 g tryptone, 5 g yeast extract, and 5 g NaCl per liter H_2O), which has a base osmolality of 260 mmol/kg as measured with a vapor pressure osmometer (Wescor Environmental). We used the osmometer to confirm that osmolarity scales linearly with osmolality across the range of concentrations used for this study, that is $c = b\,\rho$, where c is the concentration, b is the osmolality, and ρ is the density of water. Throughout this study, we express shock magnitude in terms of mM of osmolyte since molarity is what is controlled and measured experimentally.

Time-Lapse Imaging during Osmotic Shocks. Before osmotic shock experiments, overnight cultures grown in LB were diluted 1,000-fold into LB concentrated with 0–2 M sorbitol and then incubated at 37 °C until the cells were in log phase. These cultures were diluted 100-fold into prewarmed medium that contained 10 μg/mL wheat germ agglutinin (WGA) conjugated with Alexa Fluor 488 (Life Technologies) and loaded into a microfluidic flow cell (CellASIC). To ensure that cells were growing exponentially prior to the osmotic shock, the flow cell was incubated for an additional 1 h in the microscope environmental chamber (HaisonTech), which was preheated to 37 °C before cells were imaged. Before loading cells into the imaging chamber of the flow cell, the chamber was primed with growth medium using the ONIX microfluidic perfusion platform (CellASIC). While imaging, fresh medium containing WGA was perfused through the flow cell.

During osmotic shock, the medium in the flow cell was exchanged using the ONIX system. WGA was included in all perfusion media. To monitor medium osmolarity during osmotic shock, 0.5 μg/mL Alexa Fluor 647 carboxylic acid, succinimidyl ester dye (Life Technologies) was included with the concentrated medium as a tracer dye. The intensity of the tracer dye was monitored using Cy5 excitation, and osmolarity was calculated by calibrating the high and low osmolarities with the maximum and minimum fluorescence intensities, respectively.

Cell tracking was performed using custom MATLAB (The MathWorks) routines, as described in ref. (3).

Model for Growth without Envelope Softening. Approximating cell shape using a cylinder whose width $W(t)$ and length $L(t)$ change with time, we can express the position of a point parameterized by z and θ (Fig. 1) as

$$\boldsymbol{R}(\theta, z, t) = \frac{W(t)}{2}\hat{s}(\theta) + z\,L(t)\,\hat{z},\ z \in [0,1],\ \theta \in [0, 2\pi),$$

where $\hat{s}(\theta)$ and $\hat{z}$ are cylindrical basis vectors. This cylindrical ansatz, with $W(t) = W_0$ and $L(t) = L_0(t)$, is a solution of Eq. **1** (*SI Appendix*), which we interpret as the steady-state behavior of *E. coli*. When cells are perturbed away from the steady-state behavior of Eq. **1**, in the absence of softening and to linear order in deviation, the width and length behave as

$$\frac{1}{\lambda_0}\frac{d}{dt}\frac{W(t) - W_0}{W_0} \equiv \frac{1}{\lambda_0}\frac{d}{dt}\delta W(t) = g_3\delta L(0) - g_1\delta W(t), \quad [6]$$

$$\frac{1}{\lambda_0}\frac{d}{dt}\frac{L(t) - L_0(t)}{L_0(t)} = \frac{\lambda(t) - \lambda_0}{\lambda_0} \equiv \delta\lambda(t) = 2\delta L(0) + g_3\delta L(0) + g_2\delta W(t), \quad [7]$$

where $g_1 = \frac{1}{4}(\alpha_1 - \alpha_2 - 4)$, $g_2 = \frac{\alpha_2}{4}$, and $g_3 = \frac{\beta}{2}$ (*SI Appendix*).

The absence of $\delta L(t)$ from the right-hand side of Eqs. **6** and **7** can be understood since the change in length does not manifest as a change in curvature or strain, which are local quantities. As a result, growth rate does not recover in our model in the absence of softening.

At long times (steady state), the solution to Eqs. **6** and **7** is given as

$$\delta W(t \to \infty) = \frac{g_3\delta L(0)}{g_1},\ \delta\lambda(t \to \infty) = \left(2 + g_3 + g_3\frac{g_2}{g_1}\right)\delta L(0). \quad [8]$$

These results shows that width does not recover to the steady-state value in the presence of the direct strain–sensing term ($g_3 \neq 0$) and the relative change in elongation rate will not approach $2\delta L(0)$.

Model for Growth with Envelope Softening under the Stored Growth Constraint. During the period of low turgor pressure after the hyperosmotic shock, the length of the cell $L(t)$ dictated by Eq. **2** is lower than that of an unperturbed cell, $L_0(t)$. The stored growth condition demands that these two lengths are equal when pressure is restored ($p = 1$), which leads to the relation

$$\frac{\varepsilon_0}{y(t)} = \frac{L_0(t) - L(t)}{L(t) - pL_0(t)} \approx -\frac{\delta L(t)}{1-p} = \frac{\delta L(t)}{1-p}. \quad [9]$$

Thus, the value of normalized Young's modulus $y(t)=Y(t)/Y_0$ becomes a proxy for the length deviation $\delta L(t)$.

Using the relation above (Eq. **9**) in Eq. **1** to linear order in length deviation and width deviation $\delta W(t)$, we obtain

$$\frac{d}{dt}\left(\frac{\delta W(t)}{\lambda_0}\right) = -(g_1 + g_2 p)\delta W(t) - \frac{p}{1-p}\Big(g_3 - p(2+g_3)\Big)\delta L(t)$$

$$-\varepsilon_0\Big(g_3 - p(2+\Sigma)\Big), \quad [10]$$

$$\frac{d}{dt}\left(\frac{\delta L(t)}{\lambda_0}\right) = g_2(1-p)\delta W(t) - p(2+g_3)\delta L(t) + \delta L(0)(2+g_3), \quad [11]$$

Interestingly, cell-envelope softening both leads to growth-rate homeostasis ($\delta L(t \to \infty) = \text{constant}$) and enhances width homeostasis: width recovers at the faster rate $(g_1 + g_2 p)$ compared with g_1 in the case of fixed Young's modulus (Eq. **6**). This fact is consistent with our observation that the rate of width recovery after a 400-mM shock (Fig. 2*D*) is faster than after an 800-mM shock (Fig. 4*F*).

By setting the left-hand sides of Eqs. **10** and **11** to zero, we find that the solutions for length and width deviation should approach

$$\delta W(t \to \infty) = 0, \delta L(t \to \infty) = \frac{\delta L(0)}{p}. \quad [12]$$

Note that, as p approaches 0, the deviation in length increases and the equations lead to an instability when $p \leq 0$.

Data Analysis. Each curve in Figs. 2–4 and *SI Appendix*, Figs. S2–S5 was obtained by averaging over all single-cell traces after normalizing by the value at the time point immediately before the hyperosmotic shock. The unperturbed growth rate and cellular dimensions were determined from the period before the shock, from which we extrapolated the growth function $L_0(t)$. $\delta L(0)$ and $\delta W(0)$ were computed from the decrease in length and width in the 25 s directly after the shock, from which we obtained the data shown in Fig. 4*C*.

The parameters that are needed to determine the behavior of width and length in our model are g_1, g_2, g_3, and ε_0. To fit our model to experimental data, we take $\varepsilon_0 \approx 0.1$ from previous measurements (5) and minimize the error function

$$E(g_1, g_2, \Sigma) = \sum_{i=1}^{N} t_i\Big([\delta W_t(t_i) - \delta W_e(t_i)]^2 + 5[\delta L_t(t_i) - \delta L_e(t_i)]^2\Big)$$

over data points i, where the subscripts t and e refer to theoretical prediction and experimental measurement, respectively. We weighted later times more heavily since the initial conditions of the model already match the experimental data. We also weighted the length measurements fivefold more heavily since they depend on all parameters and are coupled to width; in contrast, width does not depend on the value of g_2 or length (Eqs. **6** and **7**). By minimizing this error function using simulated annealing with data for an 800-mM hyperosmotic shock, we obtained estimates of the parameters $g_1 = 4.4$, $g_2 = 7.0$, and $g_3 = 0.23$.

To assess the robustness of these values, we examined the eigenvalues and eigenvectors of the Hessian of $E(g_1, g_2, g_3)$ near this minimum. Directions in

parameter space with higher eigenvalues are expected to be more tightly constrained by the data. The eigenvalues of the Hessian (normalized by the minimum value of the function) were 164, 0.4, and 0.05, with corresponding eigenvectors $\mathbf{v}_1 = (-0.21, 0.16, 0.96)$, $\mathbf{v}_2 = (0.44, -0.86, 0.24)$, and $\mathbf{v}_3 = (0.87, 0.48, 0.11)$.

We rewrote the parameters in terms of coordinates G_1, G_2, G_3 along the eigenvectors $\mathbf{v}_1$, $\mathbf{v}_2$, and $\mathbf{v}_3$ as $g_1 = 4.4 - 0.21G_1 + 0.44G_2 + 0.87G_3$, $g_2 = 7.0 + 0.16G_1 - 0.86G_2 + 0.48G_3$, and $g_3 = 0.23 + 0.96G_1 + 0.24G_2 + 0.11G_3$. By varying the parameters G_i individually, we obtained CIs for these parameters.

In addition to fitting the parameters by the optimization procedure described above, we systematically varied the parameter values and verified the quality of the fit. Nearly all experimental results in this study were well fit by the values $g_1 = 4.4$, $g_2 = 7.0$, and $g_3 = 0.23$. For the width-dynamics data, g_2 appeared slightly overestimated, with $g_2 = 6.0$ providing a slightly better fit. We also obtained fits of $g_1 = 3.2$ and $g_2 = 5.7$ from the curvature-coupled model in the absence of strain coupling ($g_2 = 0$), approximately consistent with our other fits. In the minimal model ($g_2 = 0$, $g_3 = 0$), the value of $g_1 = 3.2$ is the same as it would be in the curvature-feedback model, since g_2 does not influence width dynamics.

Data, Materials, and Software Availability. All data are included in the manuscript and/or *SI Appendix*, or available at https://doi.org/10.7910/DVN/E1I6CF (40).

ACKNOWLEDGMENTS. The authors thank the Huang and Rojas labs for useful discussions. E.R.R. was supported by NSF CAREER award MCB-2047404. K.C.H. is a Chan Zuckerberg Biohub Investigator. K.C.H. was supported in part by the NSF grant EF-2125383. A.G. was supported in part by the NSF grant DMS-1616926; the NSF-CREST Center for Cellular and Bio-molecular Machines at University of California, Merced (HRD-1547848); and the NSF Center for Engineering Mechanobiology grant (CMMI-154857). This work was also supported in part by NSF grant PHYS-1066293 and the hospitality of the Aspen Center for Physics.

Author affiliations: [a]John A. Paulson School of Engineering and Applied Sciences, Harvard University, Cambridge, MA 02138; [b]Department of Physics, University of California, Merced, CA 95343; [c]NSF-CREST: Center for Cellular and Biomolecular Machines, University of California, Merced, CA 95343; [d]Department of Physics, Syracuse University, Syracuse, NY 13210; [e]Department of Bioengineering, Stanford University, Stanford, CA 94305; [f]Department of Microbiology and Immunology, Stanford University School of Medicine, Stanford, CA 94305; [g]Chan Zuckerberg Biohub, San Francisco, CA 94158; and [h]Department of Biology, New York University, New York, NY 10003

1. A. Amir, F. Babaeipour, D. B. McIntosh, D. R. Nelson, S. Jun, Bending forces plastically deform growing bacterial cell walls. *Proc. Natl. Acad. Sci. U.S.A.* **111**, 5778–5783 (2014).
2. H. Shi *et al.*, Deep phenotypic mapping of bacterial cytoskeletal mutants reveals physiological robustness to cell size. *Curr. Biol.* **27**, 3419–3429.e4 (2017).
3. E. Rojas, J. A. Theriot, K. C. Huang, Response of *Escherichia coli* growth rate to osmotic shock. *Proc. Natl. Acad. Sci. U.S.A.* **111**, 7807–7812 (2014).
4. A. Amir, S. van Teeffelen, Getting into shape: How do rod-like bacteria control their geometry? *Syst. Synth. Biol.* **8**, 227–235 (2014).
5. F. Chang, K. C. Huang, How and why cells grow as rods. *BMC Biol.* **12**, 54 (2014).
6. L. K. Harris, J. A. Theriot, Relative rates of surface and volume synthesis set bacterial cell size. *Cell* **165**, 1479–1492 (2016).
7. H. Shi *et al.*, Precise regulation of the relative rates of surface area and volume synthesis in bacterial cells growing in dynamic environments. *Nat. Commun.* **12**, 1975 (2021).
8. J. V. Höltje, Growth of the stress-bearing and shape-maintaining murein sacculus of *Escherichia coli*. *Microbiol. Mol. Biol. Rev.* **62**, 181–203 (1998).
9. E. C. Garner, Toward a mechanistic understanding of bacterial rod shape formation and regulation. *Annu. Rev. Cell Dev. Biol.* **37**, 1–21 (2021).
10. T. S. Ursell *et al.*, Rod-like bacterial shape is maintained by feedback between cell curvature and cytoskeletal localization. *Proc. Natl. Acad. Sci. U.S.A.* **111**, E1025–E1034 (2014).
11. T. K. Lee, K. C. Huang, The role of hydrolases in bacterial cell-wall growth. *Curr. Opin. Microbiol.* **16**, 760–766 (2013).
12. X. Yao, M. Jericho, D. Pink, T. Beveridge, Thickness and elasticity of Gram-negative murein sacculi measured by atomic force microscopy. *J. Bacteriol.* **181**, 6865–6875 (1999).
13. K. C. Huang, Y. Meir, N. S. Wingreen, Dynamic structures in *Escherichia coli*: Spontaneous formation of MinE rings and MinD polar zones. *Proc. Natl. Acad. Sci. U.S.A.* **100**, 12724–12728 (2003).
14. K. C. Huang, N. S. Wingreen, Min-protein oscillations in round bacteria. *Phys. Biol.* **1**, 229–235 (2004).
15. A. Varma, K. C. Huang, K. D. Young, The Min system as a general cell geometry detection mechanism: Branch lengths in Y-shaped *Escherichia coli* cells affect Min oscillation patterns and division dynamics. *J. Bacteriol.* **190**, 2106–2117 (2008).
16. F. Wu *et al.*, Multistability and dynamic transitions of intracellular Min protein patterns. *Mol. Syst. Biol.* **12**, 873 (2016).
17. F. Wu, B. G. van Schie, J. E. Keymer, C. Dekker, Symmetry and scale orient Min protein patterns in shaped bacterial sculptures. *Nat. Nanotechnol.* **10**, 719–726 (2015).
18. F. Wong *et al.*, Mechanical strain sensing implicated in cell shape recovery in *Escherichia coli*. *Nat. Microbiol.* **2**, 17115 (2017).
19. S. Takeuchi, W. R. DiLuzio, D. B. Weibel, G. M. Whitesides, Controlling the shape of filamentous cells of *Escherichia coli*. *Nano Lett.* **5**, 1819–1823 (2005).
20. A. Colavin, H. Shi, K. C. Huang, RodZ modulates geometric localization of the bacterial actin MreB to regulate cell shape. *Nat. Commun.* **9**, 1280 (2018).
21. S. Hussain *et al.*, MreB filaments align along greatest principal membrane curvature to orient cell wall synthesis. *eLife* **7**, e32471 (2018).
22. H. Shi, D. A. Quint, G. M. Grason, A. Gopinathan, K. C. Huang, Chiral twisting in a bacterial cytoskeletal polymer affects filament size and orientation. *Nat. Commun.* **11**, 1408 (2020).
23. B. P. Bratton, J. W. Shaevitz, Z. Gitai, R. M. Morgenstein, MreB polymers and curvature localization are enhanced by RodZ and predict *E. coli*'s cylindrical uniformity. *Nat. Commun.* **9**, 2797 (2018).
24. H. Shi, B. P. Bratton, Z. Gitai, K. C. Huang, How to build a bacterial cell: MreB as the foreman of *E. coli* construction. *Cell* **172**, 1294–1305 (2018).
25. F. Wong, E. C. Garner, A. Amir, Mechanics and dynamics of translocating MreB filaments on curved membranes. *eLife* **8**, e40472 (2019).
26. J. A. Lockhart, An analysis of irreversible plant cell elongation. *J. Theor. Biol.* **8**, 264–275 (1965).
27. W. Fricke, Turgor pressure. *eLS*, John Wiley & Sons, Ltd (Ed.), 1–6 (2017).
28. T. E. Proseus, J. S. Boyer, Calcium pectate chemistry causes growth to be stored in *Chara corallina*: A test of the pectate cycle. *Plant Cell Environ.* **31**, 1147–1155 (2008).
29. D. Roylance, *Pressure Vessels* (Department of Materials Science and Engineering, Massachusetts Institute of Technology, Cambridge, 2001).
30. S. Al Mosleh, A. Gopinathan, C. Santangelo, Growth of form in thin elastic structures. *Soft Matter* **14**, 8361–8371 (2018).
31. S. Iyer-Biswas *et al.*, Scaling laws governing stochastic growth and division of single bacterial cells. *Proc. Natl. Acad. Sci. U.S.A.* **111**, 15912–15917 (2014).
32. M. Schaechter, J. P. Williamson, J. R. Hood Jr., A. L. Koch, Growth, cell and nuclear divisions in some bacteria. *J. Gen. Microbiol.* **29**, 421–434 (1962).
33. P. Wang *et al.*, Robust growth of *Escherichia coli*. *Curr. Biol.* **20**, 1099–1103 (2010).
34. L. Willis, K. C. Huang, Sizing up the bacterial cell cycle. *Nat. Rev. Microbiol.* **15**, 606–620 (2017).
35. E. R. Rojas *et al.*, The outer membrane is an essential load-bearing element in Gram-negative bacteria. *Nature* **559**, 617–621 (2018).
36. Y. Deng, M. Sun, J. W. Shaevitz, Direct measurement of cell wall stress stiffening and turgor pressure in live bacterial cells. *Phys. Rev. Lett.* **107**, 158101 (2011).
37. A. Becskei, L. Serrano, Engineering stability in gene networks by autoregulation. *Nature* **405**, 590–593 (2000).
38. K. C. Huang, R. Mukhopadhyay, B. Wen, Z. Gitai, N. S. Wingreen, Cell shape and cell-wall organization in Gram-negative bacteria. *Proc. Natl. Acad. Sci. U.S.A.* **105**, 19282–19287 (2008).
39. L. Gan, S. Chen, G. J. Jensen, Molecular organization of Gram-negative peptidoglycan. *Proc. Natl. Acad. Sci. U.S.A.* **105**, 18953–18957 (2008).
40. S. al-Mosleh, A. Gopinathan, C. D. Santangelo, K. C. Huang, E. R. Rojas, Feedback linking cell envelope stiffness, curvature, and synthesis enables robust rod-shaped bacterial growth. Harvard dataverse. https://doi.org/10.7910/DVN/E1I6CF. Deposited 15 September 2022.